

Received July 4, 2019, accepted July 22, 2019, date of publication July 26, 2019, date of current version August 15, 2019.

Digital Object Identifier 10.1109/ACCESS.2019.2931194

# Vision-Based 3D Shape Measurement System for Transparent Microdefect Characterization

YUANLONG DENG<sup>ID</sup>, XIZHOU PAN, XINGZHENG WANG<sup>ID</sup>, (Member, IEEE),  
AND XIAOPIN ZHONG

Laboratory of Machine Vision and Inspection, College of Mechatronics and Control Engineering, Shenzhen University, Shenzhen 518060, China

Corresponding author: Xingzheng Wang (xingzheng.wang@szu.edu.cn)

This work was supported in part by the National Science Foundation of China under Grant 61571306, in part by the Shenzhen Fundamental Research fund under Grant JCYJ20160331185006518 and Grant JCYJ20180306174120445, and in part by the Startup Research Fund of Shenzhen University under Grant 2019041.

**ABSTRACT** The main task of vision-based industrial defect inspection is to implement efficient non-contact visual quality control, i.e., to detect if there is a defect and to achieve an accurate 3D shape measurement of such a defect, and this kind of vision defect inspection system has been widely applied in various industrial application. However, it is still not the case in the inspection of transparent microdefect on the polarizer (which is the most important part of an LCD screen). Optical measurement devices (such as confocal microscopy) are often utilized to fulfil this task. To solve problems lied in the current confocal microscopy inspection system, such as expensive and non-real-time processing, this research aims to develop a novel vision-based 3D shape measurement system for polarizer transparent microdefect characterization. The innovation of this system, which has been verified by our optical model simulation, is that the 3D sizes of microdefect have a monotonically relation to the grayscale of the microdefect image. Hence, a microdefect imaging system, which could acquire defect image accurately, is first well designed and implemented. Then, a support vector regression (SVR) algorithm is derived by the trained data, i.e., 100 acquired defect images and its corresponding 3D shape value by confocal microscopy. Characterized 3D measurement of microdefect is thereby obtained by this SVR algorithm. 30 polarizer microdefect samples have been imaged and measured by our proposed system, and several important performance indicators, including processing speed, accuracy and system reproducibility, have been elaborately tested. The experimental results show that the proposed system could achieve a high-accuracy measurement but in a much faster and more efficient way than the confocal microscopy. Besides, this developed imaging system has been evaluated in real applications, and over 300 samples have been detected, which also validate the effectiveness of the proposed system.

**INDEX TERMS** Machine vision, industrial defect measurement, polarizer, transparent microdefect.

## I. INTRODUCTION

Industrial vision inspection, as one of the hottest researches and application topics in computer vision and artificial intelligence, has attracts more and more attention from both the academia and the industry [1]–[8]. Many specific inspection systems have been developed and deployed in some industries such as printed circuit board (PCB) [9], [10], mobile phone glass covers processing [11], [12]. Polarizer, as one of the most important component of liquid crystal display panel

(TFT-LCD), its quality control and defect inspection has become more attentive and concerned [13], [14].

The main task of polarizer inspection system is, to detect if there is a defect, and to achieve an accurate 3D shape measurement of such a defect for further decision-making, i.e., whether this defect is small enough to be recovered automatically after the polarizer is attached to the glass plane (“*True defect*”). Some preliminary polarizer inspection systems have been developed in the past few years [15], [16], however, they can only detect if there are some type of defects but cannot decide whether it is a “*True*” or “*False*” defect. Researchers must resort to expensive optical instruments such as confocal microscopy to fulfil this task, which

The associate editor coordinating the review of this manuscript and approving it for publication was Sudhakar Radhakrishnan.

is time-consuming and non-real-time process. Therefore, it is urgent to develop a vision-based fast 3D shape measurement system for polarizer transparent microdefect characterization.

There are a few vision-based deflection measurement systems have been developed in industrial applications. Chen *et al.* [17] purposed a multi-vision deformation measuring system to extract the 3D contour of the curved plate which sized of 350 mm × 250 mm × 25 mm. Liu *et al.* [18] presented a fast rail wear measurement method based on a line structured light vision sensor. Xu *et al.* [19] proposed a rapid 3D shape measurement system based on mono-chromatic structured light patterns for Automobile industry usage. Cuypers *et al.* [20] focused on large-scale optical measurement cases about a large iron casting and double-decker train. Cao *et al.* [21] proposed a large-complex-surface surface defect detection system, and the size of detection area on the equipment cabinet surface is 500 mm × 470 mm. These systems were developed to acquire the 3D shape measurement either by multi-camera vision or structured light vision, and none of them could be applied to the measurement of polarizer defect due to its super-small size. Hence, new imaging system for 3D shape measurement of polarizer microdefect need to be further developed.

In existing research, most of the visual measurement measures the three-dimensional shape of the object through the deformation of the coded pattern, and is usually used to measure the external size [22]–[25], but for transparent internal objects, especially for micro objects, this method is not suitable. A novel vision-based fast 3D shape measurement system for polarizer transparent microdefect characterization, is elaborately researched in this work. The innovation of this measurement system is that the 3D sizes of microdefect have a monotonically relation to the grayscale of the microdefect image, which has been verified by our optical model simulation. Followed by a thorough requirement analysis for reliable rendering of all possible feature in the polarizer microdefect, a microdefect imaging system is implemented. There is the main part of this system: illuminant, lighting condition, and imaging camera have been considerably designed and developed. The proposed imaging system has two advantages, one is an easily configurable hardware-software structure and maintenance-easy, thanks to the internal independence of its components, the other is that selection and optimization of imaging system components can guide the construction of other systems. Then, a support vector regression (SVR) algorithm is derived by the obtained trained data, *i.e.*, 100 acquired defect images and its corresponding 3D shape value by confocal microscopy. Characterized 3D measurement of microdefect is thereby obtained by this SVR algorithm. Lastly, the performance of this system is carefully evaluated by several important indicators including processing speed, accuracy and system reproducibility.

The remainder of this paper is organized as follows. Section II describes the optical model simulation of system. Section III describes the structure of measurement system and corresponding requirements for each model to

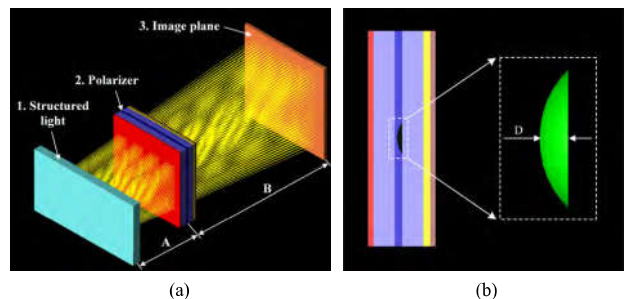


**FIGURE 1.** Optical simulation model of imaging system: (a) simulated optical path diagram; (b) defect simulation model.  $A$  is the distance from the light source to the polarizer,  $B$  is the distance from the imaging plane to the polarizer, and  $D$  is the depth value of the defect.

obtain high-quality defect images. Section IV introduces the imaging experiment and data acquisition of defects. In Section V, we conduct the performance analysis of the proposed system. Lastly, Section VI outlines the conclusion of this paper.

## II. OPTICAL MODEL SIMULATION

In the previous research, the microdefect of polarizer was equivalent to a micro-plane-convex lens model, and the illuminant finally formed a bright spot image on the imaging plane through the micro-lens. By further comparing the defect samples of different sizes, we found that the grayscale of the center of the bright spot image varies with the depth of the defect [26]–[28]. In view of this phenomenon, we proposed the assumption that there is a functional relationship between the physical depth value of the defect and the grayscale of the spot center. At the same time, we also designed optical simulation to further verify this hypothesis.

Firstly, we used TracePro [29]–[31] to simulate the defect imaging system, and then gradually changed the depth value of the defect to obtain a series of defect spot images, finally we explored the relationship between the grayscale of the bright spot image center and the physical depth value of the defect. **Fig. 1** shows the optical path diagram of the imaging system and the simulation model of defect simulated by TracePro. The simulated imaging system includes three parts: stripe structured light source, polarizer with defects and imaging plane which is equivalent to the imaging target surface of the camera.

Then, we designed a comparative experiment of defect imaging on the designed simulation imaging system. Under the condition of keeping the illuminant and optical path structure ( $A = 25$  mm and  $B = 35$  mm) unchanged, a series of bright spot image of defects with different sizes were obtained by gradually changing the depth of defects. In this simulation, we first designed six groups of comparative experiments, the depth range of defects was  $2\mu\text{m}$ – $22\mu\text{m}$ , the interval was  $4\mu\text{m}$ , so as to obtain six different bright spot image of defects. Then a group of defect-free imaging experiment was designed and compare with the other six groups of experiments. From the experimental results of defects in **Fig. 2**, this can be

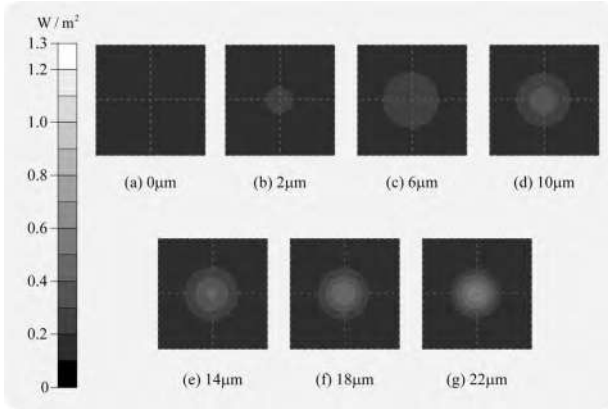


**FIGURE 2.** The bright spot diagram of defect, the size of every diagram is  $400 \mu\text{m} \times 400 \mu\text{m}$ . The depth of defect: (a)-(g)  $0 \mu\text{m}$ - $22 \mu\text{m}$ . The deeper the depth of the defect, the richer the imaging texture, respectively.

**TABLE 1.** The irradiance of the center of the defect.

No.	The depth of defect / $\mu\text{m}$	The irradiance of defect / ( $\text{W}/\text{m}^2$ )	The irradiance of background / ( $\text{W}/\text{m}^2$ )
1	0	0	
2	2	0.220	
3	6	0.259	
4	10	0.326	0.19
5	14	0.408	
6	18	0.485	
7	22	0.589	

seen that the brightness of the bright spot center of defects increases gradually with the increase of depth, and the texture of the bright spot becomes more and more abundant.

Finally, we extracted the irradiance of the center of bright spot image form the result of imaging simulation. From **Table 1**, it shows that the irradiance at the center of the spot increases with the depth of the defect, *i.e.*, from  $0.190\text{W}/\text{m}^2$  to  $0.589\text{W}/\text{m}^2$  and  $0\mu\text{m}$  -  $22\mu\text{m}$ , respectively, and the irradiance at the center of the spot is higher than that at the background. In particular, the irradiance represents only the intensity of the luminous flux in the imaging plane. What's more, the same increasing trend could be noticed from **Fig. 3**.

From these simulations, we could summarize three aspects. Firstly, combined with the simulation results of defect and imaging experiments, we can find that the irradiance of defect imaging in the simulation results is equal to the grayscale of defect image in the experiment. Secondly, the imaging results of defect are indeed related to the depth size of defects. Thirdly, the irradiance at the center of the bright spot is monotonously increasing with the depth of the defect, which can prove our previous hypothesis.

Based on the above optical simulation results, we propose that the 3D shape of the defect can be measured indirectly by using the functional relationship between the depth scale of the defect and the grayscale of image. Depending on this connection, we need to further design a complete measurement system to achieve defect measurement. Therefore, we will

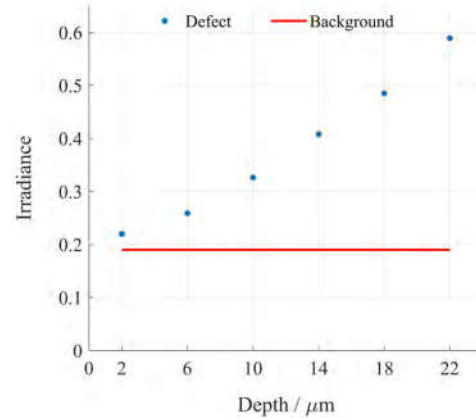


**FIGURE 3.** Irradiation of center of defects.

build a perfect imaging system to capture high-quality defect images, and use regression algorithm to establish the relationship between defect image data and physical 3D data, and finally complete the construction of the visual measurement system in Section III.

### III. VISUAL MEASUREMENT SYSTEM

Based on the optical simulation results of defect, in this section, we carefully designed and optimized the visual measurement system which can obtain high-quality defect images for the first time, which includes optical imaging system and regression algorithm. Firstly, in order to ensure high-quality defect images, we summarized the detailed imaging requirements analysis to guide the parameter optimization of each module of the imaging system, and discussed the implementation of the imaging system. Then, we selected the appropriate regression algorithm to train the defect image and physical size and got the regression model to characterize the 3D measurement of the defect.

#### A. IMAGING SYSTEM OPTIMIZATION

A typical visual imaging system, which includes three core parts: imaging camera, illuminant and optical path. In the imaging system we're going to design, it is necessary to clarify that the design of the optical path, including the illumination mode and environmental conditions, is indispensable for obtaining uniform illumination. In addition, the imaging camera needs to consider two independent parameters for resolution and grayscale bit depth to ensure that the system could obtain high quality images.

A structure of our proposed optical imaging system is clearly shown in **Fig. 4**. In this system, the imaging illuminant is provided by binary black and white stripes displayed on the TFT screen, and the defect sample is placed between the camera and the illuminant, and is backlighting. Defect images were acquired by an industrial charge coupled device (CCD) equipped with a focusing lens. A desktop computer configured for Windows 7 environment is used for image processing of defect, and the regression algorithm

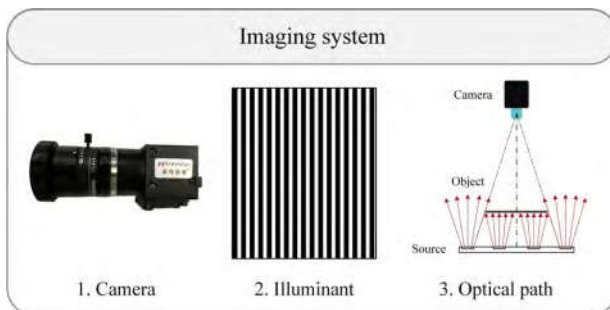


**FIGURE 4.** Framework of proposed defect vision measurement system. Three modules: imaging camera, illuminant and optical path, are essential for high quality images acquisition and accurate measurement.

and data processing we use will also run on the Windows platform.

### 1) REQUIREMENT ANALYSIS

We need to analyze and summarize the imaging characteristics of the defects on the imaging system requirements, to guide and optimized the design of the imaging system correspondingly, to obtain the best quality of the defect image. The goal of the proposed measurement method is to measure the depth size indirectly from the defect image. therefore, the captured defect image should be able to clearly highlight the texture gradient of the defect.

Obtaining high-quality, high-definition, high-stability defect images is the ultimate objective of optical imaging systems, therefore, we linked each requirement with the corresponding system module to find the appropriate standard for the design of the system. For example, to obtain a high-quality defect image, a camera with enough resolution must be selected. In addition, an illuminant with uniform brightness is required to ensure the image is clear. **Table 2** summarizes all the imaging requirements and innovative solutions that meet the vision measurement system. Next, we will detail how to select the modules of the system around these requirements.

### 2) CAMERA RESOLUTION

For imaging camera, the most important issue is to determine the minimum resolution of camera, which is related to whether the acquired image can characterize the grayscale characteristics of the defect with enough sharpness. The resolution of camera is a key parameter for the imaging system to achieve high precision measurements. In general, the higher the camera resolution, the clearer the grayscale characteristics of the defect image, but it also means more storage cost and running time. Therefore, it is necessary to find the minimum resolution of the camera that can accurately characterize the grayscale features of defects.

The resolution of the camera is closely related to the two parameters of the width of target defects and the size of the imaging field of view. In the imaging experiment of defects, we used a camera with 5.1 million pixels for

**TABLE 2.** Requirement analysis for optical imaging system.

Image features	Requirement	Problem items	Creative solution
	Resolution of camera		<ul style="list-style-type: none"> <li>Select the appropriate resolution according to the required accuracy.</li> <li>Sufficient resolution for measuring the minimum defect.</li> </ul>
	Grayscale bit depth of camera		<ul style="list-style-type: none"> <li>Adequate grayscale bit depth to characterize the depth feature.</li> </ul>
Texture gradient	High quality, clarity, stability		<ul style="list-style-type: none"> <li>High brightness uniformity illuminant.</li> <li>Adjustable, easy-to-operate illuminant.</li> </ul>
	Illuminant and optical path		<ul style="list-style-type: none"> <li>Making full use of the transparent material properties of the polarizer.</li> <li>Capturing pictures in darkroom, hood of matte material.</li> <li>Reducing human interference in the process of collecting pictures.</li> </ul>

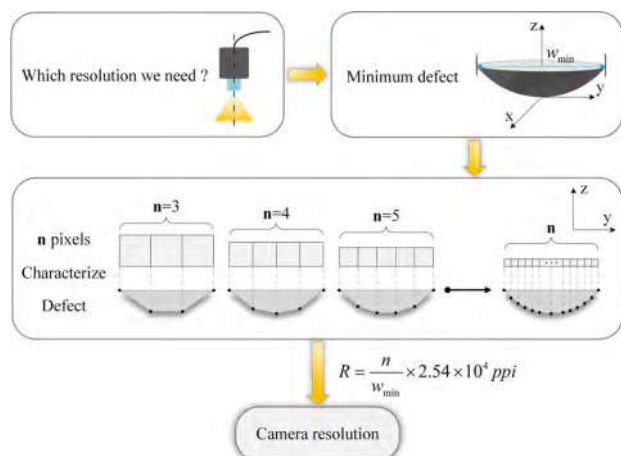


**FIGURE 5.** Visualization of pixel characterize the defect image,  $n$  is the number of pixels characterizing the defect, this is the process of showing how many pixels are required for the smallest defect.

image acquisition, and the field of view was selected as  $61.5 \text{ mm} \times 48.5 \text{ mm}$ , the width of defect samples are at least about  $200\mu\text{m}$ , and the width of the defect imaging area under this condition includes 9 pixels, and the actual resolution of the acquired defect image can be calculated as  $R = (9/200) \times 2.54 \times 10^4 \approx 1143 \text{ ppi}$ . In the calculating process of the resolution, the core question we need to explore is how many pixels are needed to characterize the smallest width of defects. In the previous study, we defined the defect as a micro-plane-convex lens model [27]. **Fig. 5** visually shows the process of  $n$  pixels characterizing the defect. The more pixels that characterize the same defect, the larger the resolution of the image acquired by the corresponding camera.

Therefore, we select the corresponding field of view according to the width of the target defect and the number of pixels characterizing the defect, and finally we can calculate the resolution of the image captured by the required camera.

Firstly, we assume that the minimum width of the target defect is  $w_{\min}$  mm, and the imaging width is characterized by  $n$  pixels, the field of view is  $L \times S$  mm. The actual resolution of the image is:

$$R = (n/w_{\min}) \times 2.54 \times 10^4 \text{ ppi} \quad (1)$$

And the size of image captured by the required camera is  $M = L \times S/R^2$  pixels. If only from the perspective of detecting the presence or absence of defects, the defect area can be characterized by one pixel, however, our goal is to obtain the depth from the grayscale characterization of defect images. Therefore,  $n$ , which is closely related to the accuracy requirements for measurement, can be determined according to the minimum size of the measured object and the size of the imaging field of view.

The above calculation process shows that we choose the resolution of the camera according to the size of the measurement defects and measurement accuracy requirements. Although we can choose a low-resolution camera, in order to ensure high-precision measurement of defects, we chose a high-resolution camera of 5.1 million pixels in the designed imaging system. This is also for the subsequent establishment of the regression model of the data prediction more accurate.

### 3) CAMERA GRayscale BIT DEPTH

The grayscale bit depth of the camera is another important issue for choosing the camera. Ideally, the more the grayscale bit depth of the camera, the more the gray level of the defect image can be characterized, and the clearer the depth texture. The appropriate grayscale bit depth of the camera is enough to characterize the grayscale characteristics of defects, which plays an extremely important role in obtaining clear images of the defect.

We assume that the depth difference between the maximum defect and the minimum defect is  $d \mu\text{m}$ , and the corresponding grayscale of defect image change  $g$  levels, so the grayscale resolution of defect images is:

$$R_g = \Delta g / \Delta d \quad (2)$$

Therefore, we could select the grayscale bit depth of camera according to the grayscale resolution of the demand and the depth range of the measured defect. The grayscale bit depth selection process of the required camera is shown in Fig. 6.

We choose an 8-bit gray industrial camera for image acquisition experiments. The specific data of defects can be found in Table 3. From this, the grayscale resolution of defects in the depth direction can be calculated as  $R_g = g/\Delta d = 140/17 \approx 8.23/\mu\text{m}$ , that is, the defect depth changes  $1\mu\text{m}$ , the grayscale of image changes 8.23 levels. Because the computer can at least distinguish one grayscale change, so the value of  $R_g$  can meet the requirements of computer grayscale resolution, that is, the 8-bit gray camera is sufficient to characterize the grayscale of defects which changes in depth  $1\mu\text{m}$ .

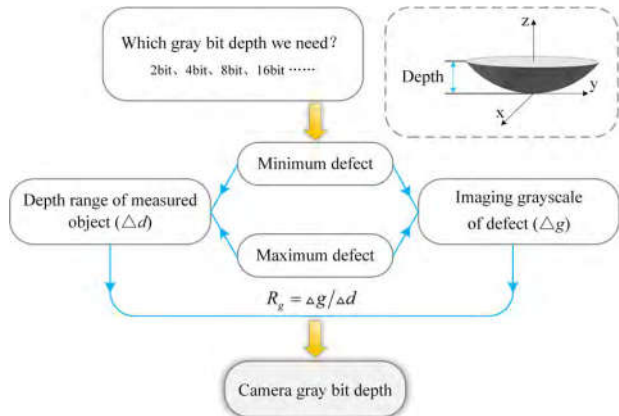


**FIGURE 6.** The flowchart for selecting the grayscale bit depth camera.

**TABLE 3.** The data of defects.

Value	Depth / $\mu\text{m}$	Imaging grayscale of defect ( $g$ )
Minimum defect	$\approx 2.7$	60
Maximum defect	$\approx 19.7$	200
Difference ( $\Delta$ )	17	140

The above discussion shows how to choose the grayscale bit depth of the camera. In addition, if we want to increase the gray level of the defect image to make the depth texture of the defect clearer, the feasible method is to select a camera with a larger grayscale bit depth, such as a 16-bit gray camera, but at the same time increase the amount of image data and the running time, or increase the exposure of the camera.

### 4) ILLUMINANT AND LIGHT PATH

The illuminant and the optical path are the two most important parts of the imaging system. A suitable illuminant would accurately reflect the grayscale characteristics of the defect image, and the best optical path could achieve uniform illumination. Therefore, the choice of illuminant and optical path is critical to obtaining clear defect images.

Firstly, the problem we should solve is what kind of illuminant to choose. The best illuminant could improve the imaging performance of defects and reduce the complexity of image processing. Structured light is widely used in three-dimensional measurement of objects [32], [33], in previous studies, we used striped structured light as an illuminant for defect imaging, which is provided by programmable binary stripes displayed on TFT-LCD. The striped structured light could effectively enhance the image contrast of the defect [26]–[28]. Therefore, we will continue to use striped structured light as the imaging illuminant of the imaging system, which is displayed on a TFT-LCD ( $1280 \times 1024$  ppi).

In addition to selecting the most suitable illuminant, the optical path plays an indispensable role in the imaging process, including lighting method and environmental

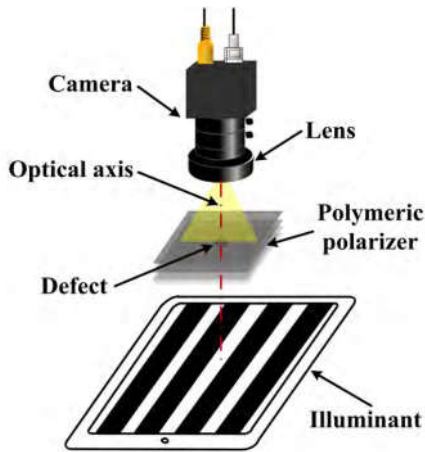


**FIGURE 7.** The imaging light path of measurement system.

conditions. As for the lighting method, one important concern is specifically how to position the illuminant and the imaging camera to achieve high-quality images. The two existing standard lighting methods are diffuse lighting and backlighting. Diffuse illumination, which is usually suitable for imaging mirror or diffuse objects, while backlighting, which is suitable for imaging transparent objects, can make the camera achieve high absorption efficiency [34]. Therefore, backlighting is the best choice for the transparency of polarizer defect. In addition, for imaging environmental conditions, we firstly consider that the imaging system must be placed in the hood to reduce the effects of ambient light. At the same time, in order to avoid the effect of light reflection from the inner wall of the hood, the inside wall should be a matte material, thus obtained defect images are robust to the change of the illuminant.

Based on the above discussion of lighting methods and environmental conditions, the optical path we proposed is shown in **Fig. 7**. An imaging system consisting of a camera, a defect sample, and an illuminant is placed in a hood, the optical axis of camera is perpendicular to the TFT monitor, and a polarizer sample placed between the camera and the TFT monitor. What's more, the imaging system needs to be positioned on a horizontal platform and reduce external mechanical vibrations and artificial interference. Satisfying the above-mentioned conditions, the imaging system could obtain high-quality defect images robustly.

### B. REGRESSION MODEL

In addition to the above imaging system, the regression model, which is designed to find a method to predict the physical depth of unknown defects by mathematical regression algorithm, it should also be included in our measurement system as a software module. Therefore, establishing a high-accuracy regression model is very important for measuring the accuracy of the system. In this section, we will focus on how to model the mathematical model between the grayscale of defect images and the physical depth to estimate

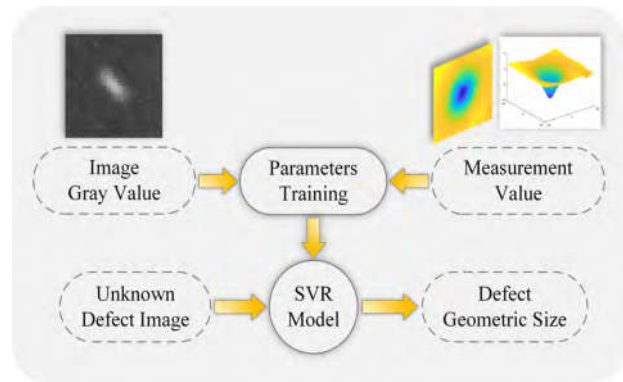


**FIGURE 8.** Framework of regression model.

the physical depth of the new defect. The frame-work for the constructed regression model is shown in **Fig. 8**. Firstly, we will capture the gray image of the defect on the built imaging system, and obtain the maximum grayscale of the bright spot center of defects, and use the confocal microscope to obtain the physical depth value of defects. Then the regression algorithm is used to train the two parts of the data to get the regression model. Finally, the 3D shape of the unknown defect is obtained by the proposed regression model.

In order to predict the defect depth of the new sample, a mathematical regression method can be used to find a regression function to describe the relationship between the grayscale of the defect image and the depth. A typical regression method is a polynomial model, but the linear model is too simple, and three or more models are prone to overfitting. Therefore, the quadratic model is a typical choice, and the true depth and estimation can be minimized by least squares and other methods. Obtained by the distance between the depths. However, methods such as least squares are susceptible to noise interference, especially the small sample problem of this study.

The SVR [35]–[38] regression model can achieve higher accuracy. SVR uses a nonlinear kernel to transform the training data into a high dimensional feature space where linear regression can be performed. The nonlinear SVR solution, using an  $\varepsilon$ -insensitive loss function

$$L_\varepsilon(y) = \max(0, |f(x) - y| - \varepsilon) \quad (3)$$

and Gaussian RBF kernel with the form,

$$K(x_i - x_j) = \exp\left(-\frac{(x_i - x_j)^2}{2\sigma^2}\right) \quad (4)$$

is given by

$$\max_{\alpha, \alpha^*} W(\alpha, \alpha^*)$$

$$= \max_{\alpha, \alpha^*} \begin{cases} -\frac{1}{2} \sum_{i=1}^l \sum_{j=1}^l (\alpha_i - \alpha_i^*)(\alpha_j - \alpha_j^*) K(x_i, x_j) \\ + \sum_{i=1}^l \alpha_i^*(y_i - \varepsilon) - \alpha_i(y_i + \varepsilon) \end{cases} \quad (5)$$

subject to the conditions,

$$0 \leq \alpha_i \leq C, \quad i = 1, 2, \dots, l \quad (6)$$

$$0 \leq \alpha_i^* \leq C, \quad i = 1, 2, \dots, l \quad (7)$$

$$\sum_{i=1}^l (\alpha_i - \alpha_i^*) = 0 \quad (8)$$

Therefore, the support vectors are exactly the points where Lagrange multipliers are greater than zero. The regression function is given by:

$$f(x) = \vec{\omega} \cdot \vec{x} + \bar{b} \quad (9)$$

where:

$$\vec{\omega} \cdot \vec{x} = \sum (\bar{\alpha}_j - \bar{\alpha}_j^*) K(x_i, x_j) \quad (10)$$

$$\bar{b} = -\frac{1}{2} \sum (\bar{\alpha}_i - \bar{\alpha}_i^*) [K(\vec{x}_r, \vec{x}_i) + K(\vec{x}_s, \vec{x}_i)] \quad (11)$$

In this paper, we choose the Gaussian Radial Basis Function (RBF) kernel and polynomial kernel to optimize the parameters. In this experiment, we utilized the library of support vector machine (lib SVR) to implement the SVR correction algorithm. There are three parameters in the RBF kernel, *i.e.*,  $C$ ,  $\sigma$  and  $\varepsilon$ .  $C$  is the penalty factor for the regression. the  $\sigma$  is the gamma of RBF kernel which determines the RBF width.  $\varepsilon$  is the factor of the lost function. Among all these three parameters, a large value of  $\sigma$  make the regression like linear regression. Furthermore, adjusting the values of  $\varepsilon$  can avoid over-fitting of regression and control the amount of support vectors. In our experiment, after optimization to achieve the lowest regression error,  $C$  is set to Infinity, and the other two are set to  $\sigma = 5$  and  $\varepsilon = 0.025$ , respectively. There are two parameters in poly-nomial kernel, *i.e.*,  $C$  for the penalty factor and  $d_0$  for the order of polynomial kernel. In our experiment, these two parameters were last set at  $C = 10$  and  $d_0 = 3$ .

#### IV. SYSTEM IMPLEMENTATION

As the software and hardware modules of measurement system have been designed in the above section, this subsection discusses how to use the imaging system to capture high-quality defect images. Also, in order to obtain an accurate regression model, we also discuss the process of obtaining training data.

##### A. IMAGE EXPERIMENT

In this subsection, after configuring all the experimental parameters in detail, we used the imaging system to capture the image of defects, and then show and describe some defect images. The structure of our vision imaging system is clearly shown in **Fig. 9**. In this imaging system, the imaging illuminant is provided by binary black and white stripes displayed on the TFT screen, and the defect sample is placed between the camera and illuminant, and is backlighting. Defect images were acquired by a plane-array CCD camera (Microvision MV-EM510M) equipped with a focusing lens

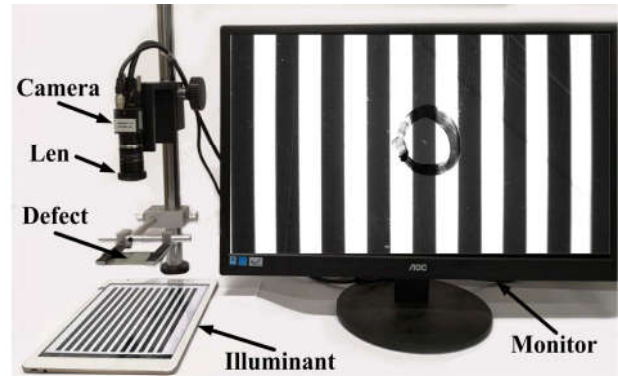


**FIGURE 9.** Vision imaging system.

**TABLE 4.** The parameters of imaging experiment.

Parameters	Values
Field of view	61.5 mm×48.5 mm
The resolution of FTF monitor	1280×1024 pixels
White stripe width	26 pixels
Black stripe width	20 pixels
Exposure time	79.0 ms
Gain	6×

(Computar 8 mm 2/3’’). A desktop computer (Inter i5-7400 3.00 GHz 8 G RAM) configured for Windows 7 environment is used for image processing of defects, and the regression algorithm and data processing we use will also run on this Windows platform.

The experiment of defect image acquisition was carried out in the hood. First, we configured the main parameters of the imaging system, including the field of view, the width of black and white stripes, and so on, which are given in **Table 4**. Keeping the conditions of experiments unchanged, we collected 100 defect images in turn, and transmitted the collected image to the computer. It is worth noting that the width of black and white stripes in stripe structured light can be matched with other combinations and the same imaging effect can be obtained.

The experimental result of image acquisition is to obtain a clear defect image data set. **Fig. 10** shows the gray image of the defect, which has obvious gray levels, there are six images that show the grayscale characteristics of defect images with depth from small to large. In particular, the region of the black circle represents the manually marked region of interest (ROI), which is intended to facilitate the location of the defect.

In **Fig. 10**, it can be observed that the shape of defects in the image is uniformly elliptical. This phenomenon does not correspond to the claim that the defect is a plane-convex lens model. Through multi-sample verification experiments, we clearly understand the reasons for this phenomenon. Because of the polarizing characteristics of the polarizer, the ray propagating in a direction parallel to the transmission

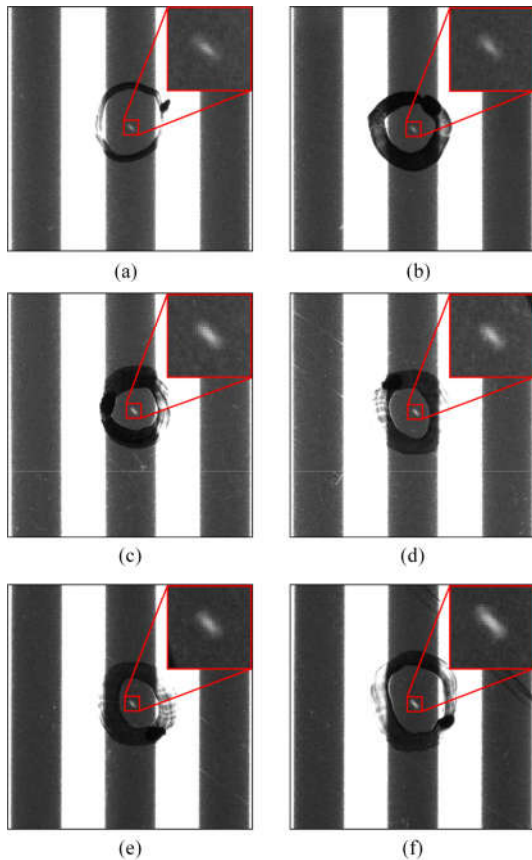


**FIGURE 10.** The images of defect samples: (a)-(f) is defect image with depth from small to large, respectively. The image size is 300 pixels×300 pixels. The red rectangle is the enlarged image of the cut defect area (30 pixels×30 pixels), and the black cycle are artificial markers used to assist in positioning.

axis can pass through the polarizer, while the light perpendicular to the transmission axis cannot pass through. The greater the angle between the propagation direction of light and the transmission axis, the lower the transmittance of the light. Therefore, the shape of the defect of the polarizer on the image is elliptical.

#### B. DATA ACQUISITION

In the proposed regression model, the input trained data includes the image grayscale of defects and the physical depth. Therefore, in this section, we discussed the process of image data and physical depth acquisition of defects in detail. We processed the collected defect images and obtain its grayscale, and we used confocal laser microscope to obtain the physical depth of the defect.

In the first step, we obtained the maximum grayscale of defect images on the MATLAB platform. **Fig. 11** shows the process from capturing images to capturing grayscale in the defect area. First, proper image smoothing is necessary for defect images, we used a Gaussian template for image smoothing to reduce noise. We used a program to automatically find the location of defects and cut the defect



**FIGURE 11.** Grayscale extraction flow chart of defect image.

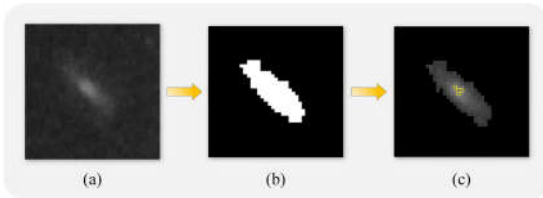


**FIGURE 12.** Flow chart of grayscale extraction of defect image. The image size is 30 pixels×30 pixels, (a) is the original image, (b) is the segmented image, and (c) is the method of extracting the grayscale of the defect, and the yellow box indicates the first four pixels with the large grayscale.

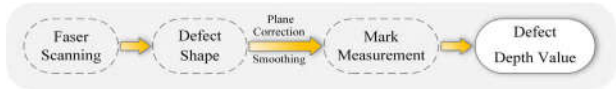


**FIGURE 13.** Flowchart for obtaining the physical depth of defects.

image as ROI (300 × 300 pixels), and then we selected the gray-scale average of the center of the black stripe as the threshold to segment the defect region, the main process is shown in **Fig. 12**. Finally, we obtained the grayscale of 100 defect samples, which is a data of regression model. Among them, it needs to be explained that we took the average grayscale of the four pixels in the defect area as the grayscale of each defect image to ensure the accuracy of the data.

In the second step, in order to ensure the accuracy of measuring the depth of defects, we used a precision measuring instrument to obtain the depth of defect. Laser confocal microscope [39], [40], as a high precision measuring instrument, is often used to measure tiny objects, and it can measure the 3D size of the internal structure of transparent thin films. Therefore, we used Keynes's laser confocal microscope (VK-X250K) to measure the depth of defects, and its depth measurement accuracy can be achieved 0.1 μm. **Fig. 13** shows a flowchart for obtaining the depth of defects using confocal microscope. Under the condition of keeping the scanning parameters unchanged, we measured the depth of 100 defect samples in turn. Firstly, we used an eyepiece (10×) and scanned each defect to obtain 3D profiles. Then, we used the microscope corresponding processing software to correct the plane of the defect contour, which can reduce the error caused by the deformation of the polarizer sample itself. **Fig. 14** shows the way to extract the depth value of the defect.

**Fig. 14** (b) shows how to measure the depth of a defect. In GB/T 3301-1999, various defects measured in depth are described in terms of the vertical distance from the deepest point to the surface. Therefore, we took the distance from

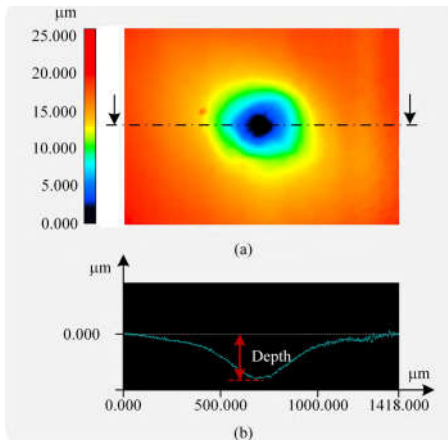


**FIGURE 14.** Laser confocal microscopy measurements: (a) a 3D profile of the defect, the dotted line is the selected cross-section. (b) The depth of the defect is extracted, where the white horizontal line is the plane-corrected reference plane.

**TABLE 5.** The result of confocal measurement error analysis.

Defect	Standard deviation ( $SD_1$ )	Average
1	0.145	
2	0.072	
3	0.053	
4	0.136	
5	0.091	
6	0.100	0.112
7	0.145	
8	0.138	
9	0.110	
10	0.128	

the lowest point of the contour to the correction plane as the depth scale of the defect artificially. In addition, there are certain errors in the manual operation method, which may affect the measurement accuracy of defect depth, so we carried out a proper error evaluation experiment. **Table 5** shows 10 defect samples using confocal microscopy to obtain depth data 5 times in a row. From the result, it can be seen that the standard deviation of manual extraction of defect depth data is less than 0.15, so errors caused by manual operations can be tolerated.

To sum up, after completing the above two steps, we have obtained the grayscale and physical depth data of 100 defect samples, so we would use the established regression model to analyze the performance of the measurement system in Section V.

## V. PERFORMANCE ANALYSIS

The hardware and software modules of the measurement system were analyzed in detail in Section 3. Performance analysis [41]–[44], an indispensable process to test the measurement quality, is proposed to ensure the robustness and stability of the proposed visual measurement system in this section. The proposed system was tested in terms of three aspects: the processing speed, the time required to measure

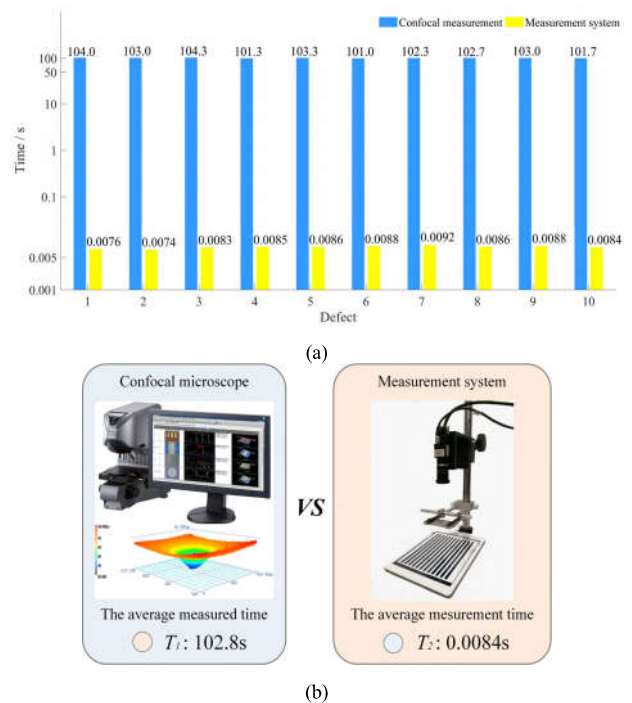


**FIGURE 15.** Comparison of measurement time: (a) comparison of 10 defect measurement times. (b) Comparison of measured average measurement time.

the depth of each defect, accuracy, the degree of deviation between the measurements of the defect and the ground truth, system consistency, which represents the reproducibility of measurements at different time points. The results of these performance analyses are as follows.

### A. PROCESSING SPEED

The processing speed is one of the most significant indicators to evaluate the character of the measurement system. In the speed test, we compare the difference in the spent time between the defect depth measured by the proposed measurement system and by laser confocal microscope to analyze the performance of the system.

In the test experiment, in order to ensure the rationality, firstly, we randomly selected 10 defect samples, and the specific location of each defect was manually marked in advance, and then under the same conditions, each unknown defect is measured in turn and the time spent was recorded. Firstly, the depth of each defect was measured using a confocal microscope, and the spent time is  $T_1$ . On the other hand, we used the imaging system to collect the gray image of each defect, the grayscale extracted from the defect is sent into the trained SVR regression model to obtain the depth measurement value, and the processing time is  $T_2$ . **Fig. 15** visually shows the specific time of each defect measured by the confocal microscope and measurement system and average measurement time. From the results of data comparison, it can be seen that the time of obtaining each defect depth by the proposed measurement system is much less

**TABLE 6.** The measurement error of defect depth.

Defect	The ground truth ( $\bar{D}$ ) / $\mu\text{m}$	Measurements ( $\bar{d}_i$ ) / $\mu\text{m}$	$AE / \mu\text{m}$	$RE / \%$
1	3.63	3.68	0.05	1.45
2	4.77	4.54	-0.23	-5.00
3	5.33	5.81	0.48	9.17
4	6.21	5.77	-0.44	-7.09
5	7.55	7.96	0.41	5.43
6	8.01	7.90	-0.11	-1.39
7	9.53	9.31	-0.22	-2.29
8	11.90	10.96	-0.94	-7.94
9	14.63	14.65	0.02	0.15
10	19.70	19.51	-0.19	-0.96

than that measured by confocal microscope, and the speed of estimating the defect depth is obviously improved.

It needs to be explained that for precision measuring instruments, the realization of high-precision measurement often means more running time, so that it is impossible to achieve a large number of automatic measuring. In contrast, our proposed measurement system only needs to send the grayscale of the defect image into the regression model to quickly estimate the defect depth. Therefore, the proposed measurement system has good advantages in measuring the 3D data of defects. In addition, the measurement speed of the system is related to the configuration of the computer, and a higher configuration can further improve the speed of defect measurement. The application of this system to the industrial automation pipeline will be able to realize the rapid estimation of the size of transparent defects on polarizers or transparent films, so as to improve the production efficiency.

### B. ACCURACY

With measurement accuracy, it means the degree of closeness between the measurement of the defect depth and the ground truth. We will use a confocal microscope to measure the depth value obtained by the defect as the ground truth, and calculate the difference between the measurements acquired by the measurement system and the ground truth of the depth to evaluate the performance of the measurement system. Firstly, we also randomly selected 10 defect samples, and the depth measurement by confocal microscope is  $D = \{D_1, \dots, D_N\}$ , and the depth of the proposed system measurement is  $d = \{d_1, \dots, d_N\}$ , where  $N$  is the number of consecutive measurements for each sample. In this test, we set  $N = 5$ , and the average values of  $N$  measurements each defect obtained by using confocal microscope measurement and measurement system are  $\bar{D}$  and  $\bar{d}_i$ , respectively. Then we calculate the absolute error ( $AE$ ) and relative error ( $RE$ ) of the defect depth measurement, which can be seen in **Table 6**. Moreover, the same measurement results can be visually seen from **Fig. 16**.

From the results of measurement accuracy, it shows that the absolute error of depth measurement of different sizes

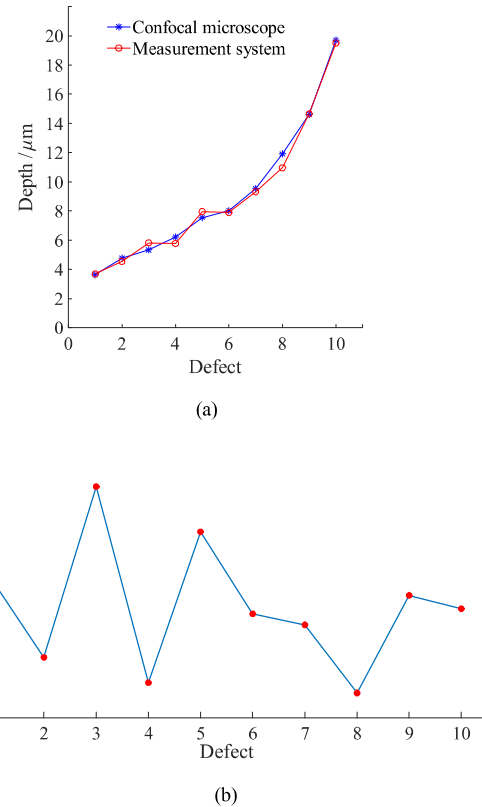


**FIGURE 16.** Measurement error of defect depth: (a) Comparison of the ground truth and measurements. (b) The relative error.

of defects are not exceed  $1\mu\text{m}$ , and the relative error is less than  $\pm 10\%$ . Usually, it is much more difficult to measure transparent defects in polarizers than opaque products, and it is much more difficult to measure internal defects than surface defects. In the existing research, Rejc *et al.* [45] proposed an automatic visual inspection system for the surface size of mechanical parts with a measurement accuracy range of less than  $\pm 20\mu\text{m}$ , Li *et al.* [46] presented a measurement method based on a two-camera vision system to measure the bayonet sizes of large automobile brake pads and the measured repeatability was  $\pm 19\mu\text{m}$ . Xiang and Zhang [47] presented a measurement method for the defect size of bearing outer ring and the maximum absolute error of measurement is  $5.4\mu\text{m}$ . The objects measured in these studies are opaque and less difficult to measure, but their measurement accuracy is lower than that of proposed measurement system, which can fully reflect the accuracy of our proposed measurement system.

### C. SYSTEM CONSISTENCY

In addition, for the consistency of the measurement system, we define the repeatability or repeatability, that is, the closeness of measurement at different points in time. We will use the proposed measurement system to measure the un-known defect sample several times continuously, the time interval of each measurement is the same, and the measurements

**TABLE 7.** The measurement error of defect depth.

Defect	Standard deviation ( $SD_2$ )	$R(\%)$
1	0.95	7.38
2	0.36	3.91
3	0.95	8.38
4	0.22	4.92
5	0.24	5.82
6	1.02	10.80
7	0.93	10.91
8	1.11	8.85
9	0.54	7.05
10	0.96	5.94
Average	0.73	7.39

of each time point is obtained. Firstly, we still randomly selected 10 defect samples, each sample was measured every minute, recorded as  $\hat{d} = \{\hat{d}_1, \dots, \hat{d}_N\}$ , the measurement time is  $N = 5$ . Based on the results of measurement experiment, there are two key definitions that can reflect the system consistency. The most common one is the standard deviation ( $SD_2$ ):

$$SD_2 = \sqrt{\sum_{i=1}^N (\hat{d}_i - \bar{d}_2)^2 / (N - 1)} \quad (12)$$

where  $\bar{d}_2$  is the average measurement of 5 times each defect. And another reference index is the ratio of the standard deviation to the mean ( $R$ ):

$$R = SD_2 / \bar{d}_2 \quad (13)$$

Based on the above calculation, the measurement consistency of the proposed system is obtained as **Table 7**. From this table, we may observe that the  $SD_2$  of multiple measurements of 10 defect samples is 0.22 to 1.11, and its average value is less than 1.00. In addition, the calculated value of  $R$  shows the measurement consistency of our system because the average value of  $R$  is only 7.39%. Based on the results of system consistency, the proposed system can maintain good stability, and can complete the task of measuring the 3D shape of polarizer defects. It is worth noting that the consistency of the system is closely related to the stability of computers, cameras, light sources and other equipment in operation, so the analysis of consistency is essential.

## VI. CONCLUSION AND DISCUSSION

This paper innovatively proposes a fast 3D shape measurement system for microdefects of polarizers, which is optimized by parameters to ensure high-quality defect images. The system is capable of quickly measuring the center depth of the polarizer defect ( $< 0.01$ s), which is 99% higher than that of the confocal microscope. At the same time, the system can achieve high measurement accuracy, compared with the confocal microscope as the ground truth of measurements, the measurement accuracy can reach about 80%, so as to accurately determine whether the polarizer indentation can be repaired by itself, and improve the production practice. And the measurement consistency error

of our system can be maintained at about 7.39%. Hence, the accuracy of defect measurement has initially met the requirements of online automation.

Of course, we propose that the measurement accuracy of the system is lower than that of other precision measurement methods. However, our goal is to provide polarizer manufacturers with guidance on defects. Defects below a certain size can disappear in the production process, and defects above a certain size cannot automatically disappear. So, this size should be an interval range rather than an accurate value. Therefore, we do not need to achieve high accuracy in the measurement of polarizer defects, and the accuracy ( $1\mu\text{m}$ ) is enough to meet the measurement of polarizer defects. Although the measurement accuracy is much lower than that of confocal microscope ( $0.1\mu\text{m}$ ), this accuracy can be used to judge whether the transparent microdefect of polarizers can be qualified in production. In addition, we also found in the experiment that adding the width and volume of defects into the training data of the regression model may improve the accuracy of the measurement. In the future, we will further study and improve the proposed measurement system.

In addition, the developed imaging system has been evaluated in practical applications and more than 300 samples have been detected and measured, which also validates the effectiveness of the proposed system. The transparent defect model studied in this paper can be extended to most film defects, which has guiding and construction significance for other optical system simulation. In addition, the research on the imaging system construction of transparent microdefects is also of guiding and critical significance for the defect measurement of other type of transparent films. Of course, due to the limitations of sample acquisition, the current experimental and test sample data sets are still small. In the future, we will also continue to increase the dataset size and establish a standardized database of polarizer defects, which will be open to the academic community for research.

## ACKNOWLEDGMENTS

The authors would like to thank the anonymous reviewers.

## REFERENCES

- [1] E. N. Malamas, E. G. M. Petrakis, M. Zervakis, L. Petit, and J.-D. Legat, "A survey on industrial vision systems, applications and tools," *Image Vis. Comput.*, vol. 21, no. 2, pp. 171–188, 2003.
- [2] C.-S. Cho, B.-M. Chung, and M.-J. Park, "Development of real-time vision-based fabric inspection system," *IEEE Trans. Ind. Electron.*, vol. 52, no. 4, pp. 1073–1079, Aug. 2005.
- [3] H. Golnabi and A. Asadpour, "Design and application of industrial machine vision systems," *Robot. Comput.-Integr. Manuf.*, vol. 23, no. 6, pp. 630–637, 2007.
- [4] S. S. Martínez, J. G. Ortega, J. G. García, A. S. García, and E. E. Estévez, "An industrial vision system for surface quality inspection of transparent parts," *Int. J. Adv. Manuf. Technol.*, vol. 68, nos. 5–8, pp. 1123–1136, 2013.
- [5] S.-H. Huang and Y.-C. Pan, "Automated visual inspection in the semiconductor industry: A survey," *Comput. Ind.*, vol. 66, pp. 1–10, Jan. 2015.
- [6] S.-H. Chen and D.-B. Perng, "Automatic optical inspection system for IC molding surface," *J. Intell. Manuf.*, vol. 27, no. 5, pp. 915–926, 2016.

- [7] Y. Peng, S. Ruan, G. Cao, S. Huang, N. Kwok, and S. Zhou, "Automated product boundary defect detection based on image moment feature anomaly," *IEEE Access*, vol. 7, pp. 52731–52742, 2019.
- [8] R. Wang, Q. Guo, S. Lu, and C. Zhang, "Tire defect detection using fully convolutional network," *IEEE Access*, vol. 7, pp. 43502–43510, 2019.
- [9] W.-C. Wang, S.-L. Chen, L.-B. Chen, and W.-J. Chang, "A machine vision based automatic optical inspection system for measuring drilling quality of printed circuit boards," *IEEE Access*, vol. 5, pp. 10817–10833, 2016.
- [10] C. Benedek, O. Krammer, M. Janoczki, and L. Jakab, "Solder paste scooping detection by multilevel visual inspection of printed circuit boards," *IEEE Trans. Ind. Electron.*, vol. 60, no. 6, pp. 2318–2331, Jun. 2013.
- [11] C. Jian, J. Gao, and Y. Ao, "Automatic surface defect detection for mobile phone screen glass based on machine vision," *Appl. Soft Comput.*, vol. 52, pp. 348–358, Mar. 2017.
- [12] J. Lei, X. Gao, Z. Feng, H. Qiu, and M. Song, "Scale insensitive and focus driven mobile screen defect detection in industry," *Neurocomputing*, vol. 294, pp. 72–81, Jun. 2018.
- [13] J. Ma, X. Ye, and B. Jin, "Structure and application of polarizer film for thin-film-transistor liquid crystal displays," *Displays*, vol. 32, no. 2, pp. 49–57, 2011.
- [14] C.-F. J. Kuo, C.-Y. Lai, C.-H. Kao, and C.-H. Chiu, "Integrating image processing and classification technology into automated polarizing film defect inspection," *Opt. Lasers Eng.*, vol. 104, pp. 204–219, May 2018.
- [15] Y.-G. Yoon, S.-L. Lee, C.-W. Chung, and S.-H. Kim, "An effective defect inspection system for polarized film images using image segmentation and template matching techniques," *Comput. Ind. Eng.*, vol. 55, no. 3, pp. 567–583, 2008.
- [16] S.-W. Sohn, D.-Y. Lee, H. Choi, J.-W. Suh, and H.-D. Bae, "Detection of various defects in TFT-LCD polarizing film," in *Adaptive and Natural Computing Algorithms*. Berlin, Germany: Springer, 2007, pp. 534–543.
- [17] F. Chen, X. Chen, X. Xie, X. Feng, and L. Yang, "Full-field 3D measurement using multi-camera digital image correlation system," *Opt. Lasers Eng.*, vol. 51, no. 9, pp. 1044–1052, 2013.
- [18] Z. Liu, J. H. Sun, H. Wang, and G. J. Zhang, "Simple and fast rail wear measurement method based on structured light," *Opt. Lasers Eng.*, vol. 49, no. 11, pp. 1343–1351, Nov. 2011.
- [19] J. Xu, N. Xi, C. Zhang, J. Zhao, B. Gao, and Q. Shi, "Rapid 3D surface profile measurement of industrial parts using two-level structured light patterns," *Opt. Lasers Eng.*, vol. 49, no. 7, pp. 907–914, 2011.
- [20] W. Cuypers, N. Van Gestel, A. Voet, J.-P. Kruth, J. Mingneau, and P. Bleys, "Optical measurement techniques for mobile and large-scale dimensional metrology," *Opt. Lasers Eng.*, vol. 47, nos. 3–4, pp. 292–300, 2009.
- [21] G. Cao, S. Ruan, Y. Peng, S. Huang, and N. Kwok, "Large-complex-surface defect detection by hybrid gradient threshold segmentation and image registration," *IEEE Access*, vol. 6, pp. 36235–36246, 2018.
- [22] H. Lin, J. Gao, Q. Mei, G. Zhang, Y. He, and X. Chen, "Three-dimensional shape measurement technique for shiny surfaces by adaptive pixel-wise projection intensity adjustment," *Opt. Lasers Eng.*, vol. 91, pp. 206–215, Apr. 2017.
- [23] S. Van der Jeugt and J. J. J. Dirckx, "Real-time structured light profilometry: A review," *Opt. Lasers Eng.*, vol. 87, pp. 18–31, Dec. 2016.
- [24] S. Zhang, "High-speed 3D shape measurement with structured light methods: A review," *Opt. Lasers Eng.*, vol. 106, pp. 119–131, Jul. 2018.
- [25] S. Zhang, "Recent progresses on real-time 3D shape measurement using digital fringe projection techniques," *Opt. Lasers Eng.*, vol. 48, no. 2, pp. 149–158, 2010.
- [26] W.-W. Lai, X.-X. Zeng, J. He, and Y.-L. Deng, "Aesthetic defect characterization of a polymeric polarizer via structured light illumination," *Polym. Test.*, vol. 53, pp. 51–57, Aug. 2016.
- [27] Y.-L. Deng, S.-P. Xu, and W.-W. Lai, "A novel imaging-enhancement-based inspection method for transparent aesthetic defects in a polymeric polarizer," *Polym. Test.*, vol. 61, pp. 333–340, Aug. 2017.
- [28] Y.-L. Deng, S.-P. Xu, H.-Q. Chen, Z.-H. Liang, and C.-L. Yu, "Inspection of extremely slight aesthetic defects in a polymeric polarizer using the edge of light between black and white stripes," *Polym. Test.*, vol. 65, pp. 169–175, Feb. 2018.
- [29] P.-C. Chang and S.-J. Hwang, "Simulation of infrared rapid surface heating for injection molding," *Int. J. Heat Mass Transf.*, vol. 49, nos. 21–22, pp. 3846–3854, 2006.
- [30] J. K. Tseng, Y. J. Chen, C. T. Pan, T. T. Wu, and M. H. Chung, "Application of optical film with micro-lens array on a solar concentrator," *Sol. Energy*, vol. 85, no. 9, pp. 2167–2178, 2011.
- [31] W.-C. Chen, K.-P. Liu, B. Liu, and T.-T. Lai, "Optimization of optical design for developing an LED lens module," *Neural Comput. Appl.*, vol. 22, nos. 3–4, pp. 811–823, 2013.
- [32] J. Geng, "Structured-light 3D surface imaging: A tutorial," *Adv. Opt. Photon.*, vol. 3, no. 2, pp. 128–160, 2011.
- [33] W. Lohry and S. Zhang, "3D shape measurement with 2D area modulated binary patterns," *Opt. Lasers Eng.*, vol. 50, no. 7, pp. 917–921, 2012.
- [34] S. S. Martínez, J. G. Ortega, J. G. García, and A. S. García, "A machine vision system for defect characterization on transparent parts with non-plane surfaces," *Mach. Vis. Appl.*, vol. 23, no. 1, pp. 1–13, 2012.
- [35] D. Basak, S. Pal, and D. C. Patranabis, "Support vector regression," *Neural Inf. Process. Lett. Rev.*, vol. 11, no. 10, pp. 203–224, 2007.
- [36] M. Cerrada, R.-V. Sánchez, C. Li, F. Pacheco, D. Cabrera, J. V. de Oliveira, and R. E. Vásquez, "A review on data-driven fault severity assessment in rolling bearings," *Mech. Syst. Signal Process.*, vol. 99, pp. 169–196, Jan. 2018.
- [37] Z. Li, Z. Zhang, J. Shi, and D. Wu, "Prediction of surface roughness in extrusion-based additive manufacturing with machine learning," *Robot. Comput.-Integr. Manuf.*, vol. 57, pp. 488–495, Jun. 2019.
- [38] A. Dai, X. Zhou, H. Dang, M. Sun, and Z. Wu, "Intelligent modeling method for a combined radiation-convection grain dryer: A support vector regression algorithm based on an improved particle swarm optimization algorithm," *IEEE Access*, vol. 6, pp. 14285–14297, 2018.
- [39] R. H. Webb, "Confocal optical microscopy," *Rep. Prog. Phys.*, vol. 59, no. 3, p. 427, 1996.
- [40] S. Fu, F. Cheng, T. Tjahjowidodo, Y. Zhou, and D. Butler, "A non-contact measuring system for in-situ surface characterization based on laser confocal microscopy," *Sensors*, vol. 18, no. 8, p. 2657, Aug. 2018.
- [41] P. Zhao, N. Gao, Z. Zhang, F. Gao, and X. Jiang, "Performance analysis and evaluation of direct phase measuring deflectometry," *Opt. Lasers Eng.*, vol. 103, pp. 24–33, Apr. 2018.
- [42] A. G. Ruggero and M. B. Enrique, "3D granulometry using image processing," *IEEE Trans. Ind. Informat.*, to be published.
- [43] F. Tombari, S. Salti, and L. Di Stefano, "Performance evaluation of 3D keypoint detectors," *Int. J. Comput. Vis.*, vol. 102, nos. 1–3, pp. 198–220, 2013.
- [44] R. S. Peres, J. Barata, P. Leitao, and G. Garcia, "Multistage quality control using machine learning in the automotive industry," *IEEE Access*, vol. 7, pp. 79908–79916, 2019.
- [45] J. Rejc, F. Kovačić, A. Trpin, I. Turk, M. Štrus, D. Rejc, P. Obid, and M. Munih, "The mechanical assembly dimensional measurements with the automated visual inspection system," *Expert Syst. Appl.*, vol. 38, no. 8, pp. 10665–10675, 2011.
- [46] C. Li, Z. Liu, and H. Xie, "A measurement method for micro 3D shape based on grids-processing and stereovision technology," *Meas. Sci. Technol.*, vol. 24, no. 4, 2013, Art. no. 045401.
- [47] R. Xiang, W. He, X. Zhang, D. Wang, and Y. Shan, "Size measurement based on a two-camera machine vision system for the bayonets of automobile brake pads," *Measurement*, vol. 122, pp. 106–116, Jul. 2018.



**YUANLONG DENG** received the B.Sc. degree from the Department of Precision Instruments and Mechanics, Tsinghua University, China, the M.Sc. degree from the National Institute of Metrology, China, and the Ph.D. degree from the College of Precision Instruments and Optoelectronic Engineering, Tianjin University, China, in 1994, 1997, and 2007, respectively. He is currently a Professor and the Director of the Laboratory of Machine Vision and Inspection, College of Mechatronics and Control Engineering, Shenzhen University, China. He has authored over 20 articles published in refereed journals and conference proceedings. His research interests include machine vision inspection, measurement technology, and instruments and sensors.

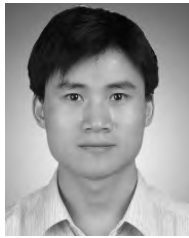


**XIZHOU PAN** received the B.Sc. degree in mechanical design, manufacture, and automation, from the College of Mechatronics and Control Engineering, Shenzhen University, China, in 2017, where he is currently pursuing the master's degree in mechanical engineering with the Laboratory of Machine Vision and Inspection, College of Mechatronics and Control Engineering. His research interests include machine vision inspection and image processing.



**XIAOPIN ZHONG** received the B.Sc. degree in automation, the M.Sc. degree in pattern recognition and intelligence from Xi'an Jiaotong University, and the Ph.D. degree in mechatronic engineering from the Ecole Centrale de Lyon, in 2002, 2007, and 2010, respectively. He is currently an Associate Professor with the Laboratory of Machine Vision and Inspection, College of Mechatronics and Control Engineering, Shenzhen University, China. He has authored over 30 articles published in refereed journals and conference proceedings. His research interests include defect inspection and 3D measurement.

• • •



**XINGZHENG WANG** received the B.Sc. degree in mechanical engineering and automation from the North China University of Technology, Beijing, China, the M.Sc. degree in mechanical engineering from Tsinghua University, Beijing, and the Ph.D. degree in computer science from Hong Kong Polytechnic University, Hong Kong, in 2004, 2007, and 2013, respectively. He has been a Postdoctoral Fellow of the Graduate School at Shenzhen, Tsinghua University, Shenzhen, China, since 2013. He is currently an Associate Professor with the College of Mechatronics and Control Engineering, Shenzhen University. His research interests include computational imaging, computer vision, and pattern recognition.